

## Field-resolved measurement of reaction-induced spectral densities by polarizability response spectroscopy

Andrew M. Moran,<sup>a)</sup> Rene A. Nome, and Norbert F. Scherer<sup>b)</sup>

*Department of Chemistry and the James Franck Institute, The University of Chicago, 929 East 57th St., Chicago, Illinois 60637, USA*

(Received 17 April 2007; accepted 10 September 2007; published online 12 November 2007)

The experimental design and theoretical description of a novel five-pulse laser spectroscopy is presented with an application to a pyridinium charge transfer complex in acetonitrile and methanol. In field-resolved polarizability response spectroscopy (PORS), an electronically resonant laser pulse first excites a solvated chromophore (reactant) and off-resonant Raman spectra of the resulting nuclear motions are measured as a function of the reaction time. The present apparatus differs from our earlier design by performing the Raman probe measurement (with fixed pulse delays) in the frequency domain. In addition, the full electric fields of the signals are measured by spectral interferometry to separate nonresonant and Raman responses. Our theoretical model shows how the PORS signal arises from nuclear motions that are displaced/driven by the photoinduced reaction. The field-resolved off-resonant (of the solute's electronic transitions) probing favors detection of solvent (as opposed to solute) dynamics coupled to the reaction. The sign of the signal represents the relative strengths of polarization responses associated with the ground and photoexcited solutions. Signatures of nonresonant and PORS signal contributions to the experimental results are analyzed with numerical calculations based on a theoretical model we have developed for reaction-induced PORS. Our model identifies two mechanisms of PORS signal generation: (i) structural relaxation induced resonance; (ii) dephasing induced resonance. In the charge transfer reaction investigated, the solvent-dependent and time-evolving (solvent) polarizability spectral density (PSD) is readily obtained. The general trend of an initial broadband inertial nuclear response followed by a decrease in the linewidth of the PSD establishes that the measured PSD is inconsistent with the approximation of a linear response. Furthermore, the explicit time evolution of the PSD is important for properly describing solvent control of reactions that do not satisfy the time-scale separability inherent to nonadiabatic kinetic models. © 2007 American Institute of Physics. [DOI: 10.1063/1.2792943]

### I. INTRODUCTION

The importance of solvent motion to chemical reactions in solutions is well established.<sup>1–10</sup> Solvent fluctuations may initiate a chemical reaction in a system by supplying sufficient kinetic energy to allow barrier crossing at a transition state. Product stabilization then involves dissipating the excess (kinetic) energy of the system through thermal contact with the solvent. Solvent dynamics occur on the subpicosecond time scale and therefore pulsed laser spectroscopies are appropriate for their experimental study. Traditional four-wave mixing spectroscopies such as transient hole burning,<sup>11–13</sup> photon echo,<sup>14–18</sup> and time resolved fluorescence Stokes shift<sup>19–23</sup> only allow making inferences about the spectrum of solute-solvent couplings (i.e., the spectral density) by monitoring properties of the solute. Furthermore, these experimental methods also only obtain the time-integrated spectral density of the process under investigation,

so the calculation of solvent influence on the reaction thus assumes the same (average) spectral density applied throughout the process.

By contrast, a new class of coherent Raman spectroscopies obtains a direct view of solvent motion in the vicinity of the solute (reactant) over the course of a reaction. Polarizability response spectroscopy (PORS) (Refs. 24–26) and resonant pump third-order Raman probe spectroscopy (RAPTORS) (Refs. 27–29) seek to measure the same dynamics, but differ substantially in implementation. The experiments are essentially a sequence of two events: (i) electronic excitation of a chromophore to initiate solvent reorganization; (ii) an off-resonant Raman probe of the resulting low-frequency nuclear motion ( $0\text{--}500\text{ cm}^{-1}$ ) of the solvent. The delay between these two events is varied to obtain the evolution of the electron-phonon coupling spectrum as the local solvent structure relaxes. Another newly developed method, femtosecond stimulated Raman spectroscopy (FSRS), can, in principle, measure the same polarization response as the PORS and RAPTORS when the actinic pump pulse and the Raman probe pulses are respectively resonant and off-resonant of the electronic transition of the

<sup>a)</sup>Present address: Department of Chemistry, The University of North Carolina at Chapel Hill, Chapel Hill, NC 27599.

<sup>b)</sup>Author to whom correspondence should be addressed. Electronic mail: nfschere@uchicago.edu.

solute (reactant).<sup>30–34</sup> However, applications of the FSRS have focused on the study of high-frequency vibrational resonances ( $>200\text{ cm}^{-1}$ ).

In this paper, we present a new experimental design and theoretical model for PORS. This work follows an earlier PORS study of solvation dynamics based on a different apparatus.<sup>24,25,35</sup> Our previous design employed heterodyne detection to separate real and imaginary signal components but did not fully resolve the signal phase. By contrast, the new method presented here uses spectral interferometry to obtain the full electric fields of the signals. In addition, the Raman probe measurement is performed in the frequency domain with fixed pulse delays, as in the FSRS,<sup>30–34</sup> to speed up data acquisition by about 300-fold. Acquisition of PORS spectral densities as a function of the reaction (or solvation) time now requires 1–3 hours versus 1 week in our previous time-domain implementation.<sup>24,25</sup> We present a theoretical model and numerical calculations to understand the signatures of nonresonant and Raman responses in the experimental PORS signal fields. The numerical calculations are compared to experimental measurements for the charge transfer complex, 1-ethyl-4-(carbomethoxy)pyridinium iodide (ECMPI), in acetonitrile (MeCN) and methanol (MeOH). This system is well suited to comparison with the theory because its negligible extinction coefficient at the frequencies of the Raman probe pulses enhances the magnitude of the solvent response relative to that of the solute.<sup>36,37</sup> Therefore, the PORS signals are dominated by motions of the solvent that are coupled to/driven by the charge transfer reaction; these are the dynamics PORS is designed to measure.

The information content of PORS is defined by its nonlinear response function, which consists of two classes of terms: those associated with the unreacting (ground) and reacting (excited) solutes.<sup>38</sup> We show that these terms enter the response function with opposite signs and therefore only nuclear motion that is coupled to the reaction contributes to the signal. A similar cancellation of terms in nonlinear response functions was observed in the early 1980s in coherent anti-Stokes Raman scattering (CARS) experiments of vapors and low-temperature solids.<sup>39–41</sup> These “dephasing-induced” resonances vanish in the absence of pure homogeneous dephasing.<sup>42</sup> Recently, Scholes and co-workers have devised an electronically resonant transient grating experiment that uses particular tensor elements to elucidate spin relaxation in CdSe quantum dots through a cancellation of terms.<sup>43–45</sup> The destructive interference in the polarization response they measure is somewhat different than that observed in PORS and CARS because it originates from the circularly polarized transition dipoles of the quantum dots; it is not intrinsic to the perturbative expansion of the density operator. For example, a system with linearly polarized transition dipoles does not exhibit this destructive interference.

A theoretical model for PORS for our new experimental implementation is presented in the following section. The polarization response is first written with finite laser pulse durations. We then assume the limiting case of line shape-limited time and frequency resolution to obtain a closed expression that captures the main features of the Raman response. Section III presents the details of our interferometer

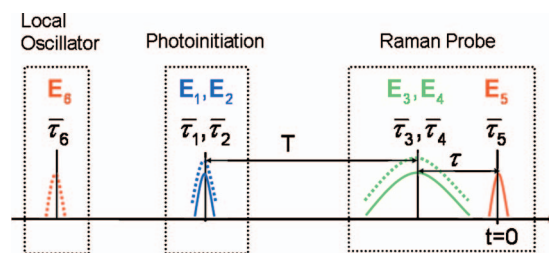


FIG. 1. (Color) The PORS temporal laser pulse configuration. Different colors are used to represent phase-related field pairs generated with a diffractive optic.  $T$  is the delay between the 1, 2 and 3, 4 field pairs. The carrier frequency of the resonant 1, 2 field pair is 405 nm, whereas the off-resonant fields 3–5 are centered near 810 nm. The 1, 2 and 5, 6 field pairs are respectively 100 and 140 fs in duration, whereas the 3, 4 pulse pair is spectrally filtered and has a duration of 700 fs. The delay between the 3, 4 field pair and field 5 is  $\tau$ . For the measurements presented in this work,  $\tau_1 = \tau_2 = T$  and  $\tau_3 = \tau_4 = \tau_5 = 0$  (i.e.,  $\tau = 0$ ). Field 5 arrives at a fixed delay with respect to the local oscillator,  $\tau_6$ .

and describes the laser pulse modulation scheme used to isolate the signal of interest. Experimental and numerical results are compared in Sec. IV to analyze signatures of nonresonant and Raman responses in the time-frequency shapes, emission times,<sup>37</sup> and real/imaginary signal components for the ECMPI/MeCN and ECMPI/MeOH systems.

## II. A THEORETICAL MODEL FOR PORS

The PORS experiment is intuitively viewed as a sequence of two events: (i) electronic excitation of a solvated chromophore; (ii) an off-resonant Raman probe of the resulting nuclear motion. This sequential picture is valid when the electronically resonant pulse and the pulses of the Raman probe are well-separated compared to their durations.<sup>38</sup> The experimental pulse sequence is presented in Fig. 2, where we indicate that the 1, 2; 3, 4; and 5, 6 field pairs are replicas (i.e., they have fixed phase relations and identical spectra). Fields 1 and 2 arrive at the sample at the same time; the same

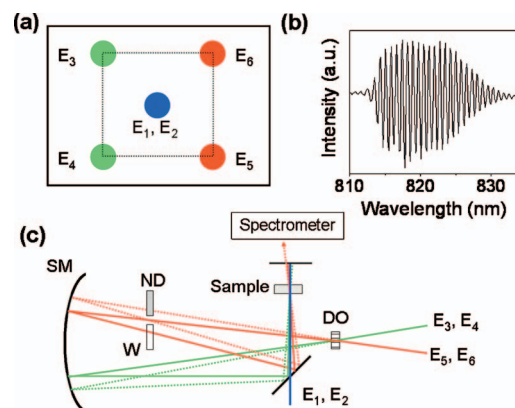


FIG. 2. (Color) (a) View of the beam geometry in front of the sample. Field pairs represented with the same colors have fixed phase relations. Fields represented with different colors are not phase related with respect to each other. (b) Interference spectrum between the PORS signal field and field 6 [see Eq. (31)]. (c) The 3, 4 and 5, 6 field pairs are focused to the same spot on a diffractive optic (DO) to generate a rectangular beam pattern that is directed to the sample with a 30 cm radius of curvature spherical mirror (SM) and a flat mirror (FM). Field 6 (i.e., the local oscillator) is attenuated with a 1 mm thick reflective BK7 neutral density filter (ND). Field 5 is delayed with respect to field 6 by a 2 mm thick  $\text{CaF}_2$  window (w).

is true for fields 3 and 4. The delay between the 1, 2 and 3, 4 field pairs is defined as  $T$  and the delay between the 3, 4 field pair and field 5 is  $\tau$  ( $\tau=0$  in the present work). Field 6 is a reference pulse used for a full signal field determination by spectral interferometry and arrives at the sample before all other pulses. The Raman probe functions in essentially the same manner as our earlier coherent Stokes Raman scattering study of pure liquids.<sup>46</sup>

### A. General and sequential polarization responses

The fundamental observable in a fifth-order nonlinear spectroscopy is the signal field,  $E_s^{(5)}(t)$ , which is related to the nonlinear polarization by

$$E_s^{(5)}(t) = \frac{i2\pi l \bar{\omega}_\tau}{n(\bar{\omega}_\tau)c} P^{(5)}(t), \quad (1)$$

where  $\bar{\omega}_\tau$  is the carrier frequency of the signal pulse and Eq. (1) assumes that the refractive index of the sample,  $n(\bar{\omega}_\tau)$ , is constant within the bandwidth of the signal. Spectroscopic techniques are defined by the pulse sequences applied to enhance particular signatures of material dynamics in  $P^{(5)}(t)$ . The electric field for a sequence of six laser pulses may be written as

$$E(\mathbf{r}, t) = \sum_{n=1}^6 [E_n(\mathbf{k}_n, t) + E_n^*(\mathbf{k}_n, t)], \quad (2)$$

where

$$E_n(\mathbf{k}_n, t) = \epsilon_n(t - \bar{\tau}_n) \exp[i\mathbf{k}_n \cdot \mathbf{r} - i\bar{\omega}_n t - i\phi_n(t)]. \quad (3)$$

In Eq. (3),  $\epsilon_n(t - \bar{\tau}_n)$  is a slowly varying envelope function for pulse  $n$  centered at time  $\bar{\tau}_n$  with carrier frequency  $\bar{\omega}_n$ , wave vector  $\mathbf{k}_n$ , and the temporal phase function  $\phi_n(t)$ .  $P^{(5)}(t)$  is

driven with five incident laser pulses. Full signal field determination is accomplished through interference of the signal with pulse 6.

The general fifth-order polarization is given by

$$P^{(5)}(t) = \int_0^\infty dt \int_0^\infty dt_5 \int_0^\infty dt_4 \int_0^\infty dt_3 \int_0^\infty dt_2 \int_0^\infty dt_1 \\ \times R^{(5)}(t_5, t_4, t_3, t_2, t_1) E_5(t - t_5) E_4(t - t_5 - t_4) \\ \times E_3(t - t_5 - t_4 - t_3) E_2(t - t_5 - t_4 - t_3 - t_2) \\ \times E_1(t - t_5 - t_4 - t_3 - t_2 - t_1). \quad (4)$$

The fifth-order response function may be written as

$$R^{(5)}(t_5, t_4, t_3, t_2, t_1) = \left(\frac{-i}{\hbar}\right)^5 \langle V | \mathcal{G}(t_5) \mathcal{V} \mathcal{G}(t_4) \mathcal{V} \mathcal{G}(t_3) \\ \times \mathcal{V} \mathcal{G}(t_2) \mathcal{V} \mathcal{G}(t_1) \mathcal{V} | \rho_{\text{eq}} \rangle, \quad (5)$$

where  $\rho_{\text{eq}}$  is the equilibrium density operator. The Liouville space Green function,  $\mathcal{G}(t)$ , and the dipole operator,  $\mathcal{V}$ , are defined by

$$\mathcal{G}(t)\rho(0) = \exp(-iHt/\hbar)\rho(0)\exp(iHt/\hbar) = \rho(t) \quad (6)$$

and

$$\mathcal{V}\rho = [V, \rho], \quad (7)$$

where  $V$  is the Hilbert space molecular dipole operator.<sup>42</sup> There are 64 terms in  $R^{(5)}(t_5, t_4, t_3, t_2, t_1)$  assuming a temporally separated  $\delta$  function field. This number increases by 5! when permutations of the electric fields are considered. The PORs response function is defined by a small subset of these terms.<sup>38</sup>

The PORs polarization response corresponding to the pulse configuration presented in Fig. 2 is given by

$$P_{\text{PORs}}^{(5)}(\mathbf{k}_s, t, \tau, T) = \int_0^\infty dt_5 \int_0^\infty dt_4 \int_0^\infty dt_3 \int_0^\infty dt_2 \int_0^\infty dt_1 R^{(5)}(t_5, t_4, t_3, t_2, t_1) E_5(\mathbf{k}_5, t - t_5 - t_4) E_4(\mathbf{k}_4, t + \tau - t_5) \\ \times E_3^*(\mathbf{k}_3, t + \tau - t_5 - t_4 - t_3) \times E_2(\mathbf{k}_2, t + \tau + T - t_5 - t_4 - t_3 - t_2) E_1^*(\mathbf{k}_1, t + \tau + T - t_5 - t_4 - t_3 - t_2 - t_1), \quad (8)$$

where  $\mathbf{k}_s = -\mathbf{k}_1 + \mathbf{k}_2 - \mathbf{k}_3 + \mathbf{k}_4 + \mathbf{k}_5$ . It is worth noting that the sequential polarization response for our earlier implementation of the PORs (Refs. 24, 25, 35, and 38) is obtained by: (i) removing  $t_4$  from the argument of pulse 5 and inserting it into the argument of pulse 4; (ii) taking pulses 3, 4, and 5 to be replicas.

### B. Approximations

The goal of this paper is to obtain physical insight into material dynamics by connecting the polarization response to experimentally accessible material parameters, e.g., vibrational frequencies and linewidths, reorganization energies, and polarizabilities. To this end, we will simplify Eq. (8) by

making five approximations: (i) the durations of the 1, 2 field pair and field 5 are short compared to the experimentally controlled delay  $T$ ; (ii) the dephasing time intervals  $t_3$  and  $t_5$  (i.e., off-resonant interactions) are much shorter than the duration of field 5 and may be removed from the electric field arguments; (iii) the durations of the 1, 2 field pair and field 5 are short compared to the time scale of nuclear dynamics; (iv) the wavelength dependence of the off-resonant Raman scattering cross section is sufficiently weak that the actual frequencies may be approximated by the average of the two frequencies intrinsic to the Raman scattering process; (v) the rotating wave approximation. The same approximations were outlined in the theoretical description of our earlier time domain implementation of the PORs.<sup>38</sup>

### C. Sequential PORS with finite pulses

Here, the approximations of Sec. II B are applied to Eq. (8) to express  $P_{\text{PORS}}^{(5)}(\mathbf{k}_s, t, \tau, T)$  in terms of experimentally accessible parameters. The first step in the PORS sequence, excitation and relaxation of the composite solute-solvent system, is described with a model for wave packet propagation originally applied to third-order pump-probe spectroscopy.<sup>42</sup> Polarizability operators are then projected onto the wave packet prepared by the 1, 2 field pair to describe the second step in the PORS sequence, the off-resonant Raman probe of nuclear motion. We show how the resulting polarization response may be parametrized with properties of the laser pulses; the linear absorption spectrum of the chromophore; the vibrational frequencies, linewidths, polarizabilities, and reorganization energies of the vibronically coupled modes.

The doorway wave packet developed in the context of a third-order pump-probe spectroscopy is given by<sup>42</sup>

$$D(\omega_1, T) \equiv \int_{-\infty}^{\infty} d\omega'_{1,2} I(\omega'_{1,2} - \omega_{1,2}) \int_0^{\infty} dt_1 [\mathcal{G}(T) \mathcal{V} \mathcal{G}(t_1) \mathcal{V} \rho_{\text{eq}}] \times \exp(i\omega'_{1,2} t_1) - \text{h.c.}, \quad (9)$$

where  $I(\omega'_{1,2} - \omega_{1,2})$  is the power spectrum of the 1, 2 field pair. Equation (9) is the convolution of  $I(\omega'_{1,2} - \omega_{1,2})$  with Mukamel's snapshot doorway wave packet and represents the case where the 1, 2 field pair is short compared to the nuclear dynamics [approx. (iii)] but not compared to optical dephasing [approx. (ii)]. Furthermore, we have assumed that  $t_2 \approx T$  [approx. (i)].

It is essential to note that  $D(\omega_1, T)$  contains terms with positive and negative signs, which are associated with the ground and excited states of the solute, respectively.<sup>38,42</sup> These terms are readily defined with Liouville space generating functions (LGFs).<sup>42</sup> The second-order LGFs are found by expanding the material part of Eq. (9),  $[\mathcal{V} \mathcal{G}(t_1) \mathcal{V} \rho_{\text{eq}}]$ , then propagating the system for  $t_2$  on either the ground or the excited state free energy surface. The four resulting LGFs are given by

$$\rho_1(t_1 + t_2) = G_{gg}(t_2) V_{ge} G_{eg}(t_1) V_{eg} \rho_{gg}, \quad (10a)$$

$$\rho_2(t_1 + t_2) = G_{gg}(t_2) G_{ge}(t_1) \rho_{gg} V_{ge} V_{eg}, \quad (10b)$$

$$\rho_3(t_1 + t_2) = -G_{ee}(t_2) G_{eg}(t_1) V_{eg} \rho_{gg} V_{ge}, \quad (10c)$$

$$\rho_4(t_1 + t_2) = -G_{ee}(t_2) V_{eg} G_{ge}(t_1) \rho_{gg} V_{ge}, \quad (10d)$$

where  $V$  and  $G$  are the Hilbert space operators and  $\rho_{gg} = \rho_{\text{eq}}$  [see Eq. (5)]. Both fields interact with either the bra or ket of  $\rho_1(t_1 + t_2)$  and  $\rho_2(t_1 + t_2)$  and therefore these LGFs cannot lead to excitation of the system. By contrast, one interaction occurs with the bra and one with the ket of  $\rho_3(t_1 + t_2)$  and  $\rho_4(t_1 + t_2)$ , thereby transforming the density operator from  $\rho_{gg}$  to  $\rho_{ee}$ . It should be noted that the LGFs,  $\rho_i(t_1 + t_2)$ , depend separately on the two time arguments and not on their sum.<sup>42</sup> The four LGFs of Eq. (10a)–(10d) are the “roots” of all terms in the full fifth-order PORS response function, which are obtained by further expansion of the density operator. We

have explicitly presented the 16 terms in the PORS response function elsewhere.<sup>38</sup>

Equation (9) may be written as a nuclear wave packet in a coordinate space by assuming parabolic (harmonic) free energy surfaces, the overdamped limit of nuclear relaxation, and the static limit of line broadening.<sup>42</sup> The wave packet is given by

$$D_j^m(q_j, T) = \frac{1}{\delta q_j(T) \sqrt{2\pi}} \exp\left[-\frac{(q_j - q_j^m(T))^2}{2\delta q_j^2(T)}\right], \quad (11)$$

where  $j$  is an index for the nuclear mode  $q_j$ ,  $m$  denotes the electronic state of the solute, and  $q_j^m(T)$  and  $\delta q_j^2(T)$  are the delay-dependent position and variance, respectively, of the wave packet when the solute is in state  $m$ .  $D_j^g(q_j, T)$  arises from the  $\rho_1(t_1 + t_2)$  and  $\rho_2(t_1 + t_2)$  theLGFs, whereas  $\rho_3(t_1 + t_2)$  and  $\rho_4(t_1 + t_2)$  give rise to  $D_j^e(q_j, T)$ . Therefore, as shown below, these wave packets enter the full response function with opposite signs.<sup>38</sup> The position and width of the wave packet are

$$q_j^m(T) = \frac{\lambda_j + (\omega_0 - \omega_{eg}^0 - \lambda_j) M_j(T)}{\sqrt{2\lambda_j \omega_j}} \quad (12)$$

and

$$\delta q_j^2(T) = \frac{1}{\beta \omega_j} \left[ 1 - \frac{2\lambda_j}{2\lambda_j + \beta \delta \omega_{1,2}^2} M_j^2(T) \right], \quad (13)$$

where  $\omega_j$  is the frequency of mode  $j$ ,  $M_j(T)$  describes the dynamics of nuclear relaxation,  $\lambda_j$  is the reorganization energy of mode  $j$  with respect to the two electronic levels of the solute,  $\beta$  is the Boltzmann factor (i.e.,  $\beta = 1/kT$ ), and

$$\omega_0 = \frac{2\lambda_j \omega_{1,2}}{2\lambda_j + \beta \delta \omega_{1,2}^2} + (\omega_{eg}^0 + \lambda_j) \frac{\delta \omega_{1,2}^2}{2\lambda_j + \delta \omega_{1,2}^2}. \quad (14)$$

Equations (15) and (16) assume the 1, 2 field pair has a Gaussian spectrum with the center frequency  $\omega_{1,2}$  and variance  $\delta \omega_{1,2}^2$  [see Eq. (9)].

The description of the PORS polarization response requires projecting polarizability operators onto  $D_j^m(q_j, T)$ . The polarizability operator is defined as

$$\alpha(\omega_{pr}) \equiv \int_0^{\infty} dt [\mathcal{V} \mathcal{G}(t) \mathcal{V}] \exp(i\omega_{pr} t) - \text{h.c.}, \quad (15)$$

where  $\omega_{pr} = \frac{1}{2}(\omega_3 + \omega_5)$  [approx. (iv)]. The frequency dependence of  $\alpha(\omega_{pr})$  is very weak within the bandwidth of the laser pulses for samples that are transparent with respect to fields 3, 4, and 5. Therefore, we hereafter omit  $\omega_{pr}$  from the argument of  $\alpha(\omega_{pr})$ .

The nonequilibrium PORS correlation function can now be written in a basis of discrete nuclear modes as<sup>38</sup>

$$\Phi_j^m(t_4, T) = \frac{i|\mu_{eg}|^2}{\hbar^5} \langle [\alpha_j(0), \alpha_j(t_4)] D_j^m(q_j, T) \rangle, \quad (16)$$

where  $\alpha_j(t)$  is the polarizability operator for mode  $j$ . It is important to note that  $\Phi_j^m(t_4, T)$  depends on the spectrum of the resonant 1, 2 field pair through Eq. (9), whereas  $R^{(5)}(t_5, t_4, t_3, t_2, t_1)$  [Eq. (5)] is a purely material function. Equation (19) resembles the third-order coherent Raman

scattering response function obtained under similar approximations. The third-order polarizability susceptibility is given by<sup>47</sup>

$$\chi_{\alpha\alpha}^{(3)}(t) = \frac{-i}{\hbar} \langle [\alpha(t), \alpha(0)] \rho_{\text{eq}} \rangle. \quad (17)$$

The fundamental difference between Eqs. (16) and (17) is that the polarizabilities are projected onto the equilibrium density operator in Eq. (17), whereas they are projected onto the nonequilibrium doorway wave packet in Eq. (16). The form of Eq. (16) and its close relation to Eq. (17) enhances physical insight. Furthermore, Eq. (16) is a useful representation because the further manipulations shown below make use of the analytical tools developed in the context of four-wave mixing spectroscopies.<sup>42</sup>

The assumption of linear response and Lorentzian line shapes for the Raman bands yields<sup>38</sup>

$$\begin{aligned} \Phi_j^m(t_4, T) &= \frac{i|\mu_{eg}|^2}{\hbar^5} [1 - \exp(-\beta\hbar\omega_j)] \\ &\times \exp[(i\omega_j - \Gamma_j^m)t_4] \int_{-\infty}^{\infty} dq_j |\alpha_j(q_j^m)|^2 D_j^m(q_j, T). \end{aligned} \quad (18)$$

The effects of finite frequency resolution are incorporated by convoluting  $\Phi_j^m(t_4, T)$  with the finite duration pulses of the Raman probe

$$\begin{aligned} P_{\text{PORS}}^{(5)}(t, \tau, T) &= E_4(t + \tau) \int_{-\infty}^{\infty} dt_4 \sum_j [\Phi_j^g(t_4, T) - \Phi_j^e(t_4, T)] \\ &\times E_3^*(\tau + t - t_4) E_5(t - t_4). \end{aligned} \quad (19)$$

We next introduce the quasi-instantaneous electronic nonlinearity of the solution to compute realistic signals at short pulse delays,  $T$ . The nonresonant responses of liquids generally give rise to broadband signal emission when the pulses are overlapped in the sample.<sup>37,46,48</sup> By taking all field-matter interactions in Eq. (4) to occur simultaneously, the nonresonant polarization response can be written as

$$P_{\text{NR}}^{(5)}(t, \tau, T) = E_5(t) E_4(t + \tau) E_3^*(t + \tau) E_2(t + \tau + T) E_1^*(t + \tau + T). \quad (20)$$

The total polarization response

$$P_{\text{tot}}^{(5)}(t, \tau, T) = P_{\text{NR}}^{(5)}(t, \tau, T) + P_{\text{PORS}}^{(5)}(t, \tau, T) \quad (21)$$

is a linear combination of the vibrationally resonant PORS and nonresonant contributions.

## D. Model for line shape-limited time-frequency resolution

In this section, we present a simplified expression for the PORS polarization response in the limit that (i) the 1, 2 field pair and field 5 are temporal  $\delta$  functions and (ii) the 3, 4 field pair is monochromatic. The effect on  $\Phi_j^m(t_4, T)$  of assuming the 1, 2 pulse pair has infinite bandwidth is found by taking  $\delta\omega_{1,2}^2$  to be infinite in Eqs. (11)–(13). Next, we modify Eq. (19) by replacing  $E_5(t-t_4)$  with the  $\delta$  function  $\delta(t-t_4)$  and

setting  $E_3(t-t_4) = E_4(t-t_4) = \exp(i\bar{\omega}_{3,4}t)$ , where  $\bar{\omega}_{3,4}$  is the carrier frequency of the 3, 4 field pair. The resulting expression is further simplified by defining the nonequilibrium correlation function

$$Y_j^m(t_4, T) = \Phi_j^m(t_4, T) \delta[q_j^m(T) - q_j], \quad (22)$$

where the  $\delta$  function,  $\delta[q_j^m(T) - q_j]$ , restricts the integral in Eq. (18) to the maxima of the wave packets. The polarization response for this limiting case is given by

$$P_{\text{PORS}}^{(5)}(\omega_{rs}, T) = \int_{-\infty}^{\infty} \sum_j [Y_j^g(t, T) - Y_j^e(t, T)] \exp[-i\omega_{rs}t], \quad (23)$$

where  $\omega_{rs} = \bar{\omega}_{3,4} - \omega_r$ .

$P_{\text{PORS}}^{(5)}(\omega_{rs}, T)$  is rewritten in terms of our model parameters as

$$P_{\text{PORS}}^{(5)}(\omega_{rs}, T) = \sum_j c_j \left[ \frac{\alpha(0)^2}{\omega_{rs} - \omega_j + i\Gamma_j^g} - \frac{\alpha[\Delta q_j(T)]^2}{\omega_{rs} - \omega_j + i\Gamma_j^e} \right], \quad (24a)$$

where

$$c_j = \frac{|\mu_{eg}|^2}{\hbar^5} [1 - \exp(-\beta\hbar\omega_j)] \quad (24b)$$

and

$$\Delta q_j(T) = \frac{2\lambda_j [1 - M_j(T)]}{\sqrt{2\lambda_j\omega_j}}. \quad (24c)$$

The origins of the PORS response are particularly clear in Eqs. (24a)–(24c). *The two mechanisms of PORS signal generation are: (i) structural relaxation induced resonance; (ii) dephasing induced resonance.*<sup>38</sup> The definition of structural relaxation induced resonance is clarified by assuming that  $\Gamma_j^g = \Gamma_j^e$ . If  $\Gamma_j^g = \Gamma_j^e$ , then  $P_{\text{PORS}}^{(5)}(\omega_{rs}, T)$  is nonzero only for modes with nonzero reorganization energies,  $\lambda_j$ . Thus, only modes displaced by the reaction contribute to the signal. Furthermore,  $\Delta q_j(T)$  contains two terms with opposite signs; the consequence is that signal strength is predicted to increase as the solvent structure relaxes following electronic excitation of the solute (i.e., initiation of the reaction). Finally, the key to mechanism (i) is that the polarizability,  $\alpha[\Delta q_j(T)]$ , is coordinate dependent, otherwise the two terms in  $P_{\text{PORS}}^{(5)}(\omega_{rs}, T)$  would cancel for all values of  $T$ . Dephasing induced resonance occurs when  $\Gamma_j^g \neq \Gamma_j^e$ , which allows  $P_{\text{PORS}}^{(5)}(\omega_{rs}, T)$  to be nonzero even if the reorganization energy is zero.<sup>39–41</sup>

Figure 3 illustrates the physical process underlying Eqs. (24a)–(24c). The experiment begins when the electronically resonant pulse,  $E_{1,2}$ , interacts with the equilibrium system to create ground and excited state populations, which are associated with the terms on the left and right in Eq. (24a). Reorganization of the solvent structure surrounding the excited system is described by evolution of the coordinate  $\Delta q_j(T)$  [Eq. (24c)]. The solvent structure surrounding the ground state solute molecules does not relax in  $T$  because  $E_{1,2}$  is taken to be a temporal  $\delta$  function (i.e., ground state wave packet amplitude is not allowed to develop). The final step in

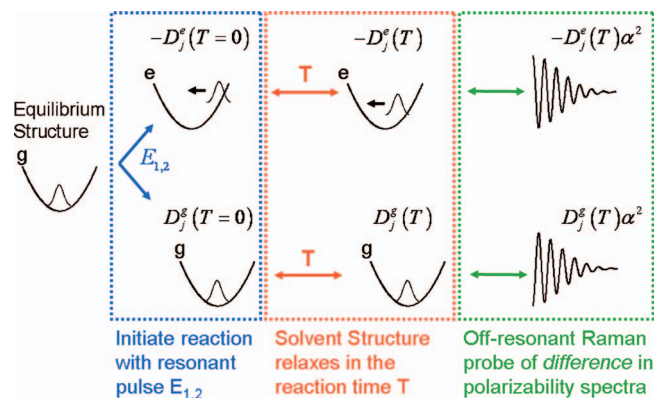


FIG. 3. (Color) Schematic for the sequence of events involved in generating the PORS signal. An electronically resonant pulse,  $E_{1,2}$ , first initiates a reaction in a solute to create ground and excited state wave packets,  $D_j^g(T)$ . The nonequilibrium solvent structure surrounding the excited system relaxes in the reaction time,  $T$ . The difference in Raman spectra of the solvent for the two pathways is measured at the pulse delay  $T$  because the ground and excited state polarization responses are  $180^\circ$  out-of-phase.

the experiment occurs at time  $T$  when the difference in the polarizability spectra for the two populations is measured with an off-resonant Raman probe pulse sequence (see Fig. 1). Figure 3 emphasizes that the interaction of the system with the resonant pulse,  $E_{1,2}$ , is the origin of the  $180^\circ$  out-of-phase polarization responses. Equations (10a)–(10d) shows that this interference arises from an even and odd number of field-matter interactions occurring with the ket for ground and excited state terms, respectively.<sup>38</sup>

### III. EXPERIMENTAL CONSIDERATIONS

#### A. Signal detection by spectral interferometry

The present measurement approach is valid when fields 3–6 are off-resonant with respect to electronic transitions of the solution, including transient absorption of the excited state of ECMPI produced by excitation with fields 1 and 2. We have confirmed that a transient absorption signal is not measured in a pump-probe configuration in which the solution is pumped at 405 nm and probed at 810 nm. However, while transient resonances of ECMPI may be nonabsorptive at 810 nm, they can still contribute to the measured dynamics through the wings of their dispersive line shapes.<sup>36,49,50</sup> Therefore, we seek to measure only the imaginary part of Eq. (24a)–(24c), which is  $90^\circ$  out-of-phase with signal fields that are associated with the dispersive wings of the solute's resonances. This is accomplished by measuring the full electric field of the signal.

Spectral interferometry is used to determine the full electric field of the signal.<sup>51–54</sup> As indicated in Fig. 2, the signal and local oscillator (field 6) are automatically collinear after the sample because the field pair generated with the diffractive optic gives the correct phase matching geometry. The total interference spectrum,  $I_{\text{tot}}(\omega_t, \tau, T, \bar{\tau}_6)$ , is given by<sup>55–57</sup>

$$I_{\text{tot}}(\omega_t, \tau, T, \bar{\tau}_6) = \left| \int_{-\infty}^{\infty} dt [E_s^{(5)}(t, \tau, T) + E_6(t - \bar{\tau}_6)] \exp(i\omega_t t) \right|^2, \quad (25)$$

where  $E_s^{(5)}(t, \tau, T)$  is defined in Eq. (1). We note that  $\omega_t$  is conjugate to  $t$ , where  $t=0$  is defined as the time the peak of

field 5 arrives at the sample (see Fig. 1).  $I_{\text{tot}}(\omega_t, \tau, T, \bar{\tau}_6)$  is Fourier transformed with respect to  $\omega_t$  to allow filtering the signal and local oscillator intensities,  $|E_s(\mathbf{k}_s, t, \tau, T)|^2 + |E_6(\mathbf{k}_s, t - \bar{\tau}_6)|^2$ , in the time domain (i.e., a dc offset). The complex cross term of Eq. (25) is then expressed as<sup>58,59</sup>

$$I_{SI}[\omega_t, \tau, T; \psi(\omega_t)] = \hat{\xi}_s(\omega_t, \tau, T) \hat{\xi}_6(\omega_t) \exp\{i[\psi(\omega_t) - \omega_t \bar{\tau}_6]\}, \quad (26)$$

where  $\hat{\xi}_j(\omega_t, T, \tau) = \xi_j(\omega_t, T, \tau) \exp[i\mathbf{k}_j \cdot \mathbf{r}]$  and  $\psi(\omega_t)$  is the phase difference between the signal and local oscillator,  $\psi(\omega_t) = \varphi_s(\omega_t) - \varphi_6(\omega_t)$ . Equation (26) oscillates at a frequency determined by the delay of field 5 with respect to field 6,  $\bar{\tau}_6$  (see Fig. 1). An example of  $I_{SI}[\omega_t, \tau, T; \psi(\omega_t)]$  is shown in Fig. 2(b). The signal field is found by obtaining values for the three parameters of Eq. (26): the delay,  $\bar{\tau}_6$ , is acquired by Fourier transforming an interferogram of fields 5 and 6; the power spectrum of the local oscillator,  $|\hat{\xi}_6(\omega_t)|^2$ , is measured while all other fields are blocked; the phase of the local oscillator,  $\varphi_6(\omega_t)$ , is calibrated by performing a PORS experiment with the pure solvent (the pure solvent is exchanged for the solution without moving the flow cell). Dividing Eq. (26) by  $\hat{\xi}_6(\mathbf{k}_6, \omega_t)$  and  $\exp(-i\omega_t \bar{\tau}_6)$  then adding  $\varphi_6(\omega_t)$  to  $\psi(\omega_t)$  gives the signal field

$$E_s(\omega_t, \tau, T) = \hat{\xi}_s(\omega_t, T) \exp[i\varphi_s(\omega_t)]. \quad (27)$$

We take the phase of the signal for a pure transparent solvent at  $T = \tau = 0$  to be  $\pi/2$  for our parametrization of  $\varphi_s(\omega_t)$ .<sup>36</sup>

#### B. Passive phase stabilization

The technical issues associated with detecting the PORS signal field are similar to those discussed in Ref. 46 where we demonstrated that the signal phase for coherent Stokes Raman emission with a four-pulse beam geometry is inherently stabilized by cancellations between the phases of two field pairs generated with a diffractive optic. The full field determination capability of PORS is based on similar considerations of the beam geometry and the use of two phase-related field pairs. The phase stability of the interferometer is passive in that the phase calibration procedure described in the previous subsection is performed and no further adjustments are made.

The PORS signal is emitted in the phase-matched direction  $\mathbf{k}_s = -\mathbf{k}_1 + \mathbf{k}_2 - \mathbf{k}_3 + \mathbf{k}_4 + \mathbf{k}_5$ , which corresponds to the signal phase

$$\varphi_{SI} = [\varphi_2 - \varphi_1] + [\varphi_4 - \varphi_3] + [\varphi_5 - \varphi_6] + \varphi_s. \quad (28)$$

The key to passive phase stability is to design the experiment so that fluctuations between phases in the three bracketed terms cancel. The utility of diffractive optics for this purpose was first demonstrated in four-wave mixing experiments.<sup>60–62</sup>

Our experimental beam geometry and interferometer are presented in Fig. 2. The first two field-matter interactions occur with a single laser pulse in our experiment so the cancellation of the  $[\varphi_2 - \varphi_1]$  term in Eq. (28) is trivial. We achieve cancellations in the second and third terms of Eq. (28) by deriving the 3, 4 and 5, 6 field pairs from the  $\pm 1$

diffraction orders produced with a diffractive optic. These two field pairs are “phase-locked” or phase related, meaning that the two pulses of a particular field pair have identical phase fluctuations. Therefore, cancellation of the  $[\varphi_4 - \varphi_3]$  and  $[\varphi_5 - \varphi_6]$  terms is also obtained. The long term phase stability is  $\pm 5^\circ$  over several hours and is primarily limited by temperature stability (drift) in the laboratory. A feedback algorithm for active phase stabilization of the interferometer is unnecessary.<sup>63</sup>

### C. Isolating the signal of interest

The beam geometry uses a single electronically resonant laser pulse rather than two noncollinear beams to excite the chromophore. Therefore, a third-order signal associated with the Raman probe is emitted in the same direction as the PORS signal. Furthermore, additional third-order signals may contribute when the electronically resonant field(s) arrives before field 6 (i.e., when  $T > 1$  ps). In this section, we show how these lower order and unwanted optical signals can be removed by modulating the amplitudes of the pulses.

Four third-order polarization responses emit fields in the same phase matched direction as the PORS signal. Assuming the beam geometry given in Fig. 2, these terms are specified by their wave vectors as

$$S_1^{(3)}: \mathbf{k}_s = -\mathbf{k}_3 + \mathbf{k}_4 + \mathbf{k}_5, \quad (29a)$$

$$S_2^{(3)}: \mathbf{k}_s = -\mathbf{k}_1 + \mathbf{k}_2 + \mathbf{k}_6, \quad (29b)$$

$$S_3^{(3)}: \mathbf{k}_s = -\mathbf{k}_3 + \mathbf{k}_3 + \mathbf{k}_6, \quad (29c)$$

$$S_4^{(3)}: \mathbf{k}_s = -\mathbf{k}_4 + \mathbf{k}_4 + \mathbf{k}_6. \quad (29d)$$

$E_6(\mathbf{k}_6, t)$  does not interact with a polarization induced by  $E_5(\mathbf{k}_5, t)$  because these two fields are well-separated compared to their durations (see Fig. 2).

All undesired third-order polarization responses can be removed by modulating two beams. We choose to modulate the electronically resonant beam,  $E_1(\mathbf{k}_1, t)$  and  $E_2(\mathbf{k}_2, t)$ , and the beam that generates the  $E_3(\mathbf{k}_3, t)$ ,  $E_4(\mathbf{k}_4, t)$  field pair before it reaches the diffractive optic (see Fig. 2). The total signal field should be considered under four conditions: (i)  $E_1(\mathbf{k}_1, t)$  &  $E_2(\mathbf{k}_2, t)$  ON /  $E_3(\mathbf{k}_3, t)$  &  $E_4(\mathbf{k}_4, t)$  ON; (ii)  $E_1(\mathbf{k}_1, t)$  &  $E_2(\mathbf{k}_2, t)$  OFF /  $E_3(\mathbf{k}_3, t)$  &  $E_4(\mathbf{k}_4, t)$  ON; (iii)  $E_1(\mathbf{k}_1, t)$  &  $E_2(\mathbf{k}_2, t)$  ON /  $E_3(\mathbf{k}_3, t)$  &  $E_4(\mathbf{k}_4, t)$  OFF; (iv)  $E_1(\mathbf{k}_1, t)$  &  $E_2(\mathbf{k}_2, t)$  OFF /  $E_3(\mathbf{k}_3, t)$  &  $E_4(\mathbf{k}_4, t)$  OFF. These four conditions yield the four total signal fields

$$S_i^{\text{Total}} = S_1^{(3)} + S_2^{(3)} + S_3^{(3)} + S_4^{(3)} + I_{\text{het}}[\omega_r, \tau, T; \psi(\omega_r)] + |E_6(\mathbf{k}_6, t)|^2 + |E_s(\mathbf{k}_s, t)|^2, \quad (30a)$$

$$S_{ii}^{\text{Total}} = S_1^{(3)} + S_3^{(3)} + S_4^{(3)} + |E_6(\mathbf{k}_6, t)|^2, \quad (30b)$$

$$S_{iii}^{\text{Total}} = S_2^{(3)} + |E_6(\mathbf{k}_6, t)|^2, \quad (30c)$$

$$S_{iv}^{\text{Total}} = |E_6(\mathbf{k}_6, t)|^2. \quad (30d)$$

The experimental interference spectrum is found by computing  $S_{\text{PORS}} = S_i^{\text{Total}} - S_{ii}^{\text{Total}} - S_{iii}^{\text{Total}} + S_{iv}^{\text{Total}}$  or equivalently  $S_{\text{PORS}} = I_{\text{SI}}[\omega_r, \tau, T; \psi(\omega_r)] + |E_s(\mathbf{k}_s, t)|^2 - |E_s(\mathbf{k}_s, t)|^2$  can then be nu-

merically filtered in the time domain to isolate the interferogram  $I_{\text{SI}}[\omega_r, \tau, T; \psi(\omega_r)]$  (see Sec. III A).

A simpler modulation scheme can be used for the special case when  $E_6(\mathbf{k}_6, t)$  arrives at least 1 ps before  $E_5(\mathbf{k}_5, t)$ ; the pulse durations of the  $E_1(\mathbf{k}_1, t)$ ,  $E_2(\mathbf{k}_2, t)$  and  $E_5(\mathbf{k}_5, t)$ ,  $E_6(\mathbf{k}_6, t)$  field pairs are 100 fs or less; the bandwidth of the  $E_3(\mathbf{k}_3, t)$ ,  $E_4(\mathbf{k}_4, t)$  field pair is greater than  $20 \text{ cm}^{-1}$ . Under these conditions,  $S_3^{(3)}$  and  $S_4^{(3)}$  do not contribute to the signal because the  $E_3(\mathbf{k}_3, t)$ ,  $E_4(\mathbf{k}_4, t)$  field pair arrives after (and is well separated from)  $E_6(\mathbf{k}_6, t)$ . Furthermore,  $S_2^{(3)}$  does not contribute when  $T < 800$  fs because  $E_1(\mathbf{k}_1, t)$ ,  $E_2(\mathbf{k}_2, t)$  arrives after  $E_6(\mathbf{k}_6, t)$ . In this special case,  $S_i^{\text{Total}} - S_{ii}^{\text{Total}} = I_{\text{SI}}[\omega_r, \tau, T; \psi(\omega_r)] + |E_s(\mathbf{k}_s, t)|^2$ .

### D. Details of implementation

Our experiments are performed with a home built 1 kHz Ti:Sapphire laser system<sup>59</sup> and the interferometer presented in Fig. 2(a). Briefly, the 3, 4 and 5, 6 field pairs are generated by filtering the laser system fundamental in all-reflective 4F pulse stretchers aligned for zero dispersion. Fields 1, 2 are obtained as the second harmonic of the laser system (405 nm). As shown in Fig. 2, the beams form a square pattern after the diffractive optic (DO), where the angle between the  $\pm 1$  diffraction orders is  $5.0^\circ$  at 800 nm. Pulse energies at the sample are 400 nJ/pulse for the electronically resonant beam [200  $\mu\text{m}$  full width at half maximum (FWHM) spot size] and 200 nJ/pulse for pulses 3–5 (100  $\mu\text{m}$  FWHM spot sizes). The sample is contained in a 1 mm path length flow cell with an optical density of 0.3 at 400 nm. The signal and local oscillator pulses, which are collinear after the sample, are focused into a 0.32 m monochromator (Jobin-Yvon TRIAX 320), dispersed with a 600 g/mm grating (blazed at 450 nm) and imaged on a charge coupled device array detector (Hamamatsu S7032-1007). The electronically resonant pulse is modulated at 10 Hz with a mechanical shutter (Thorlabs). The chemical reaction time,  $T$ , is less than 1 ps for all measurements reported here and the bandwidth of the 3–4 field pair is  $25 \text{ cm}^{-1}$ , which allows the PORS signal to be isolated by computing  $S_i^{\text{Total}} - S_{ii}^{\text{Total}}$  (see Sec. III C).

## IV. COMPARISON OF THEORETICAL AND EXPERIMENTAL SIGNALS

In this section, theoretical calculations are compared to experimental measurements for the ECMPI charge transfer complex in acetonitrile (MeCN) and methanol (MeOH) to identify signatures of  $P_{\text{PORS}}^{(5)}(t, \tau, T)$  and  $P_{\text{NR}}^{(5)}(t, \tau, T)$  in the measured signal fields. Parameters of the theoretical model are given in Table I. These values are chosen because they roughly reproduce the experimental signals for  $T > 150$  fs. The coordinate dependence of the polarizability assumed here is discussed in Appendix A. The 1, 2 and 3, 4 field pairs are taken to be Gaussian functions with 100 and 700 fs FWHM durations. The form of field 5 is given in Appendix B. The experimental and theoretical spectra of the Raman probe fields are presented in Fig. 4(a). Figure 4(b) shows the temporal profiles of the theoretical laser pulses.

TABLE I. Summary of model parameters.

Parameters <sup>a</sup>	Value
$\omega_1$	60 cm <sup>-1</sup>
$\lambda_1$	500 cm <sup>-1</sup>
$\Gamma_1^g$	0.005 fs <sup>-1</sup>
$\Gamma_1^e$	0.005 fs <sup>-1</sup>
$\alpha'[q_j^m(T)]^b$	1.0–0.01 $q_1$

<sup>a</sup>The parameters are defined in Eq. (18). The solvation correlation function is given by  $M_j(T) = 0.75 \exp(-T/0.05) + 0.25 \exp(-T/0.25)$ .

<sup>b</sup>See Appendix A for the definition.

### A. Real and imaginary signal components

Absorptive and dispersive polarization responses are 90° out-of-phase and are therefore separable as real and imaginary signal components, respectively. For  $P_{\text{PORS}}^{(5)}(t, \tau, T)$ , the real component represents the line shape of the vibrational resonance(s), whereas the imaginary component is related to the Kramers–Kronig transform of the real component; the Kramers–Kronig relation is exact under the approximations of Sec. II D. By contrast, the line shape of  $P_{\text{NR}}^{(5)}(t, \tau, T)$  depends only on the temporal profiles of the laser pulses and their convolution [see Eq. (20)].

Real and imaginary experimental PORS signal components of ECMPI in MeCN are presented in Figs. 5(a) and 5(b), respectively. A comparison of these spectra reveals that the real (absorptive) component has a slightly narrower linewidth than the imaginary (dispersive) component. In addition, the real component decays more slowly in  $T$  than the imaginary component. The difference in linewidths is anticipated since the bandwidth of  $P_{\text{NR}}^{(5)}(t, \tau, T)$ , which dominates

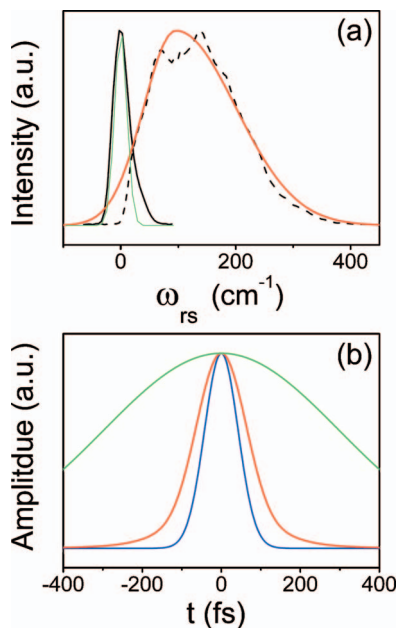


FIG. 4. (Color) (a) Experimental (solid black) and theoretical (green) spectra of the 3, 4 field pair, where the theoretical spectrum is taken to be a Gaussian with a FWHM of 25 cm<sup>-1</sup>. Experimental (dashed black) and theoretical (red) spectra of field 5, where the theoretical spectrum is computed as discussed in Appendix B. The experimental spectrum of field 5 is centered at 810 nm. The Raman shift is defined as  $\omega_{rs} = \bar{\omega}_{3,4} - \omega_l$ . (b) Temporal profiles of the 1, 2 field pair (blue); the 3, 4 field pair (green); the 5, 6 field pair (red). The 1, 2 field pair is Gaussian in form with a 100 fs FWHM.

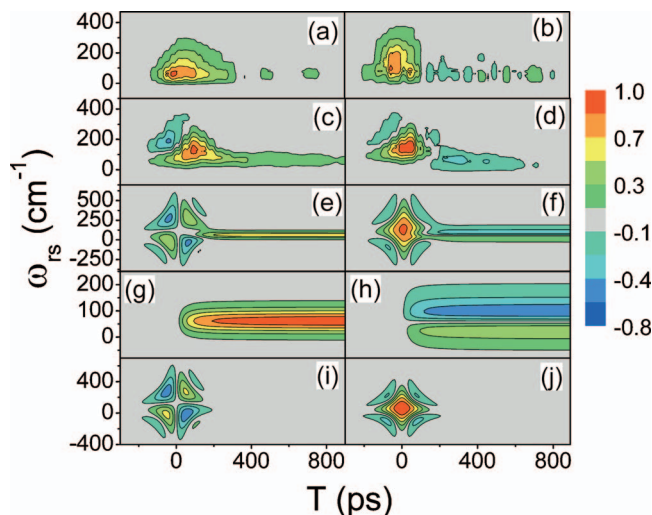


FIG. 5. (Color) Experimental (a) real and (b) imaginary PORS signal components for ECMPI in MeCN [Eq. (32)]. Experimental (c) real and (d) imaginary PORS signal components for ECMPI in MeOH [Eq. (32)]. Theoretical (e) real and (f) imaginary signal components of  $P_{\text{tot}}^{(5)}(t, \tau, T)$  computed with Eqs. (24a)–(24c). Theoretical (g) real and (h) imaginary signal components of  $P_{\text{PORS}}^{(5)}(t, \tau, T)$  computed with Eq. (22). Theoretical (i) real and (j) imaginary signal components of  $P_{\text{NR}}^{(5)}(t, \tau, T)$  computed with Eq. (23). All calculations use the parameters given in Table I. The data within each row are normalized to the maximum value for that pair of spectra.

the imaginary signal component at short  $T$ , is limited only by the laser pulse durations, whereas the bandwidth of  $P_{\text{PORS}}^{(5)}(t, \tau, T)$  is determined by the finite dephasing times of the material's vibrational resonances. A similar difference in signal bandwidths was recently observed in third-order field resolved coherent Raman experiments with pure liquids.<sup>46</sup> The different time scales for relaxation in  $T$  also follows from the fact that  $P_{\text{NR}}^{(5)}(t, \tau, T)$  vanishes when the applied fields are not temporally overlapped in the sample [Eq. (20)], whereas the relaxation time scale of  $P_{\text{PORS}}^{(5)}(t, \tau, T)$  in  $T$  depends only on the material properties [Eq. (19)].

Figures 5(c) and 5(d) respectively present the real and imaginary experimental signal components of ECMPI in MeOH. In contrast to the real spectra of ECMPI/MeCN given in Fig. 5(a), the real component exhibits a sign change at negative  $T$  with positive amplitude at lower values of the Raman shift. Similar features were observed at negative  $T$  in field-resolved transient grating measurements for electronically resonant systems.<sup>36,37,59</sup> This sign change represents a quasi-instantaneous response in the region of the pulse convolution. As  $T$  increases, the amplitude becomes completely positive and the spectral content shifts to lower frequencies. The experimental imaginary component exhibits a similar sign change to that observed for the real component at negative  $T$ ; the amplitude becomes completely positive near  $T = 0$  then changes sign again near  $T = 200$  fs. Similar to the real component in Fig. 5(c), the spectral content shifts to lower frequencies as  $T$  increases.

The theoretical real and imaginary components of  $P_{\text{tot}}^{(5)}(t, \tau, T)$  are displayed in Figs. 5(e) and 5(f). The real component exhibits a similar sign change in amplitude at negative  $T$  to that observed experimentally for ECMPI in MeOH. However, the sign change is inverted at positive  $T$ .

This is a signature of a gating effect between the resonant 1, 2 field pair and field 5, which arises from the instantaneous response of  $P_{\text{NR}}^{(5)}(t, \tau, T)$ . The real component becomes completely positive and centered at  $60 \text{ cm}^{-1}$  for  $T > 250 \text{ fs}$ . By contrast, the imaginary component is sharply peaked and possesses all positive amplitude near  $T=0$ . It exhibits a dispersive line shape (i.e., a Kramers–Kronig transform of the real part) centered at  $60 \text{ cm}^{-1}$  for  $T > 250 \text{ fs}$ .

$P_{\text{tot}}^{(5)}(t, \tau, T)$  is decomposed into  $P_{\text{PORS}}^{(5)}(t, \tau, T)$  and  $P_{\text{NR}}^{(5)}(t, \tau, T)$  in Figs. 5(g)–5(j). It is clear that  $P_{\text{NR}}^{(5)}(t, \tau, T)$  dominates the signal emission near  $T=0$ , whereas  $P_{\text{PORS}}^{(5)}(t, \tau, T)$  contributes at larger values of  $T$  when the pulses are no longer temporally overlapped.  $P_{\text{PORS}}^{(5)}(t, \tau, T)$  is zero for  $T < 0$  by approximation (i) of Sec. II B. Therefore, the rise of  $P_{\text{PORS}}^{(5)}(t, \tau, T)$  in  $T$  may be underestimated by Eq. (21). Our experimental data for both systems [Figs. 5(a)–5(d)] do not exhibit the sign change associated with  $P_{\text{NR}}^{(5)}(t, \tau, T)$  at short positive  $T$ , which suggests that  $P_{\text{PORS}}^{(5)}(t, \tau, T)$  dominates the signal in this range of  $T$  in the experiment. It is interesting that the real spectra for the ECMPI/MeCN and ECMPI/MeOH solutions respectively do and do not exhibit the theoretically predicted sign change associated with  $P_{\text{NR}}^{(5)}(t, \tau, T)$  at negative  $T$ . The rise of  $P_{\text{PORS}}^{(5)}(t, \tau, T)$  in  $T$  is apparently faster in MeCN than in MeOH; Eq. (27) shows that this difference arises from faster relaxation of the local solvent structure for MeCN than for MeOH. We further explore the consequences of the different solvent dynamics on reaction rates in another publication.<sup>26</sup>

## B. Time-frequency shapes

Time-frequency representations were first used in experimental four-wave mixing investigations during the last decade.<sup>53,54,64</sup> As discussed above, recent technical advances in experimental designs<sup>60,65</sup> and field-resolved detection methods<sup>51–54</sup> have allowed for robust measurements of electric fields at optical wavelengths in nonlinear spectroscopies. We have recently examined signal fields with this representation in studies of chemical reaction dynamics,<sup>36,59,66</sup> solute and solvent signal field resolution<sup>37</sup> and high-frequency Raman responses of pure liquids.<sup>46</sup> These studies have found that signatures of resonant and nonresonant responses are readily identified in the spectrograms of the signal fields.

Figure 6 presents experimental signal fields [Eq. (27)] that have been transformed into spectrograms using<sup>55</sup>

$$\Sigma(\omega, t) = \left| \int_{-\infty}^{\infty} E_s(\tau) g(t - \tau) \exp(-i\omega\tau) d\tau \right|^2, \quad (31)$$

where  $g(t - \tau)$  is taken to be a Gaussian function with a FWHM of 100 fs. There are clear differences in the evolution of the signal fields for the two systems. The emission time (i.e., peak of the projection onto time axis) for ECMPI/MeOH is delayed with respect to that of ECMPI/MeCN at  $T=0 \text{ fs}$ . We reiterate that  $t=0 \text{ fs}$  is defined as the time field 5 arrives at the sample (see Fig. 1). The emission times become similar for  $T \geq 100 \text{ fs}$ . However, the data show significant differences in the spectral content for the two systems at these pulse delays. The spectral content evolves toward lower vibrational frequencies in ECMPI/MeOH compared to

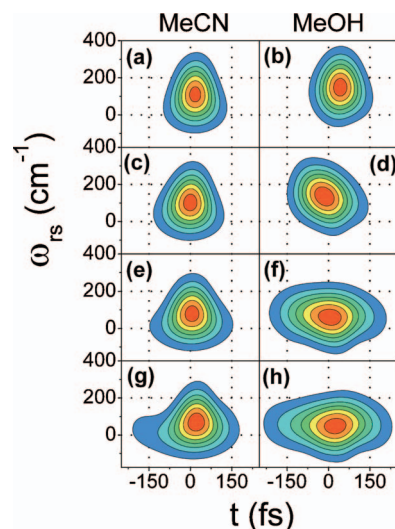


FIG. 6. (Color) Experimental PORS signal spectrograms processed with Eq. (31). PORS signal spectrograms for the ECMPI/MeCN and ECMPI/MeOH solutions at  $T=0 \text{ fs}$  are given in (a) and (b), respectively. PORS signal spectrograms for the ECMPI/MeCN and ECMPI/MeOH solutions at  $T=100 \text{ fs}$  are given in (c) and (d), respectively. PORS signal spectrograms for the ECMPI/MeCN and ECMPI/MeOH solutions at  $T=200 \text{ fs}$  are given in (e) and (f), respectively. PORS signal spectrograms for the the ECMPI/MeCN and ECMPI/MeOH solutions at  $T=300 \text{ fs}$  are given in (g) and (h), respectively.

ECMPI/MeCN as  $T$  increases from 100 to 300 fs. In addition, the signal field duration is 1.2–1.5 times greater for ECMPI/MeOH than for ECMPI/MeCN.

Signatures of  $P_{\text{PORS}}^{(5)}(t, \tau, T)$  and  $P_{\text{NR}}^{(5)}(t, \tau, T)$  [see Eq. (21)] are decomposed in the theoretical spectrograms presented in Fig. 7. Parameters used in these computations are given in Table I. The spectrograms associated with  $P_{\text{NR}}^{(5)}(t, \tau, T)$  exhibit a decrease in the time of signal emission as  $T$  increases. By contrast, the time-frequency shapes of  $P_{\text{PORS}}^{(5)}(t, \tau, T)$  are essentially independent of the pulse delay,  $T$ .  $P_{\text{tot}}^{(5)}(t, \tau, T)$  is a superposition of these two polarization responses.  $P_{\text{NR}}^{(5)}(t, \tau, T)$  dominates  $P_{\text{tot}}^{(5)}(t, \tau, T)$  at  $T=0 \text{ fs}$ , whereas  $P_{\text{PORS}}^{(5)}(t, \tau, T)$  dominates  $P_{\text{tot}}^{(5)}(t, \tau, T)$  for  $T \geq 200 \text{ fs}$ .  $P_{\text{PORS}}^{(5)}(t, \tau, T)$  and  $P_{\text{NR}}^{(5)}(t, \tau, T)$  are of similar magnitude at  $T=125 \text{ fs}$  and strongly interfere; the signal field possesses a narrow pulse width limited feature associated with  $P_{\text{PORS}}^{(5)}(t, \tau, T)$  at  $T=-80 \text{ fs}$  followed by a trailing exponential decay in  $t$  that arises from  $P_{\text{PORS}}^{(5)}(t, \tau, T)$ . Similar interference effects between resonant and nonresonant polarization responses were discussed in the context of field-resolved coherent Stokes Raman scattering experiments with pure liquids.<sup>46</sup>

Inspection of Fig. 7 reveals that the bandwidths of the theoretical signals exceed that of field 5 [see Fig. 4(a)]. The calculated signal bandwidth is determined by Eq. (20), where field 5 is multiplied by the shorter duration fields 1 and 2. To illustrate this concept, Fig. 4(b) displays the temporal pulse configuration used to compute  $P_{\text{NR}}^{(5)}(t, \tau, T)$  in Fig. 7(c). It is clear that  $P_{\text{NR}}^{(5)}(t, \tau, T)$ , which is a simple product of these fields, must have a shorter duration than field 5 alone. This is a purely nonresonant effect.  $P_{\text{PORS}}^{(5)}(t, \tau, T)$  does not exceed the bandwidth of field 5 because its finite response time is limited by the inverse linewidths of the vibrational reso-

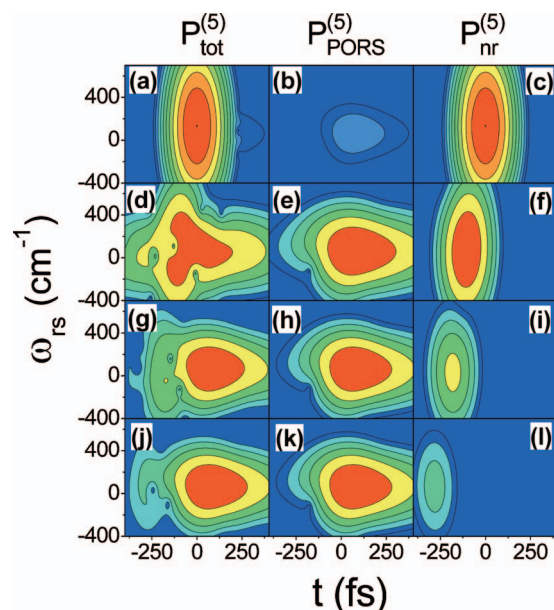


FIG. 7. (Color) Theoretical PORS signal spectrograms computed with Eq. (31) and the parameters in Table I. Signal fields arising from  $P_{\text{tot}}^{(5)}(t, \tau, T)$ ,  $P_{\text{PORS}}^{(5)}(t, \tau, T)$  and  $P_{\text{NR}}^{(5)}(t, \tau, T)$  at  $T=0.1$  fs are given in (a), (b), and (c), respectively; at  $T=125$  fs are given in (d), (e), and (f), respectively; at  $T=200$  fs are given in (g), (h), and (i), respectively; at  $T=300$  fs are given in (j), (k), and (l), respectively. The magnitudes of the spectrograms in each row are plotted on the same logarithmic scale, where each contour lines represents a different decade. There are 10 decades in the first row and 6 decades in the second, third, and fourth rows.

nances, which are 200 fs for the present model (see Table I). Therefore, the vibrational frequency associated with  $P_{\text{PORS}}^{(5)}(t, \tau, T)$  is well defined by its Raman shift with respect to the frequency of the 3, 4 field pair. The present experiment is insensitive to the larger bandwidth of  $P_{\text{NR}}^{(5)}(t, \tau, T)$  because field 6 is a replica of field 5; signals are not detected at frequencies where the amplitude of field 6 is negligible [see Eq. (26)].

### C. Emission times

Our previous four-wave mixing studies have shown that the delay in signal emission for resonant polarization responses directly reflects the bandwidths of transient electronic resonances (i.e., wave packet dynamics).<sup>36,59,66</sup> Emission times increase as transition linewidths become narrower by way of a Kramers–Kronig relation between the absorptive and dispersive components of the polarization response; the slope of the spectral phase is the delay in the signal emission time. Similarly, the bandwidth of  $P_{\text{PORS}}^{(5)}(t, \tau, T)$  reflects the distribution of the reorganization energy among various nuclear motions; the concentration of reorganization energy within a narrow frequency range results in a narrow signal bandwidth which in turn gives rise to a greater delay in the time of signal emission.

The experimental emission times,  $t_{\text{em}}$ , displayed in Fig. 8(a) are computed with

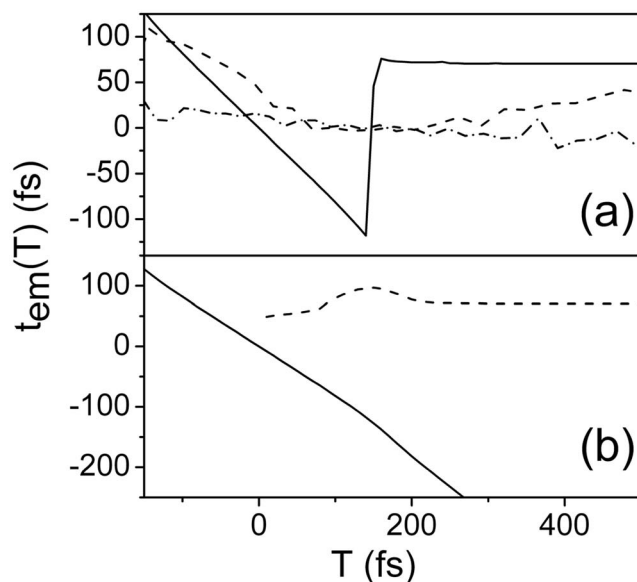


FIG. 8. (a) Experimental signal emission times,  $t_{\text{em}}(T)$  [Eq. (32)], obtained for ECMPI in MeCN (dashed-dotted black) and MeOH (dashed black). Theoretical  $t_{\text{em}}(T)$  computed with  $P_{\text{tot}}^{(5)}(t, \tau, T)$  (solid black). (b) Theoretical  $t_{\text{em}}(T)$  calculated for  $P_{\text{PORS}}^{(5)}(t, \tau, T)$  (dashed black) and  $P_{\text{NR}}^{(5)}(t, \tau, T)$  (solid black). The theoretical  $t_{\text{em}}(T)$  are computed with the parameters given in Table I.

$$t_{\text{em}}(\tau=0, T) = \frac{\int_{-\infty}^{\infty} t |E_s(t, \tau, T)| dt}{\int_{-\infty}^{\infty} |E_s(t, \tau, T)| dt}, \quad (32)$$

where  $\tau=0$  for all measurements and calculations. The emission times for ECMPI in MeCN decrease monotonically with increasing  $T$ . By contrast, the emission times for ECMPI in MeOH initially decrease at negative  $T$  then increase for delays greater than  $T=200$  fs. The emission times computed for  $P_{\text{tot}}^{(5)}(t, \tau, T)$  are also presented in Fig. 8(a). As in the experimental data,  $t_{\text{em}}(T)$  exhibits a negative slope with respect to  $T$  near  $T=0$ . The value of  $t_{\text{em}}(T)$  then increases sharply near  $T=200$  fs and converges to a constant value of  $t_{\text{em}}(T) = 70$  fs. The calculation captures the main features of the experimental observation, but does not exhibit a smooth transition from  $P_{\text{NR}}^{(5)}(t, \tau, T)$  near  $T=0$  to  $P_{\text{PORS}}^{(5)}(t, \tau, T)$  for  $T > 200$  fs. Approximation (i) of Sec. II B causes this deviation between experiment and theory near  $T=0$ .

Emission times computed for  $P_{\text{PORS}}^{(5)}(t, \tau, T)$  and  $P_{\text{NR}}^{(5)}(t, \tau, T)$  are presented in Fig. 8(b). The emission times of  $P_{\text{PORS}}^{(5)}(t, \tau, T)$  converge to a constant value by  $T=200$  fs, whereas those of  $P_{\text{NR}}^{(5)}(t, \tau, T)$  decrease linearly with increasing  $T$ . A similar effect has also been observed in recent heterodyned transient grating measurements.<sup>37,48,67</sup> The signal generation mechanism can be understood by considering the electronic nonlinearity of the liquid to respond instantaneously to the applied fields. Therefore,  $t_{\text{em}}(T)$  follows the convolution of the laser pulses (see Fig. 4 of Ref. 37). Note that  $t_{\text{em}}(T)$  of  $P_{\text{tot}}^{(5)}(t, \tau, T)$  is not the average of the  $t_{\text{em}}(T)$ 's for  $P_{\text{NR}}^{(5)}(t, \tau, T)$  and  $P_{\text{PORS}}^{(5)}(t, \tau, T)$  because the amplitudes of the latter two components are  $T$  dependent (see Fig. 7).

The calculated  $t_{\text{em}}(T)$  suggest that the signals measured for ECMPI/MeCN are dominated by  $P_{\text{PORS}}^{(5)}(t, \tau, T)$  at all  $T$ . By contrast, the experimental signals of ECMPI/MeOH ex-

hibit a clear evolution from  $P_{\text{NR}}^{(5)}(t, \tau, T)$  to  $P_{\text{PORS}}^{(5)}(t, \tau, T)$  with increasing  $T$ . Equation (24a) shows that  $P_{\text{NR}}^{(5)}(t, \tau, T)$  dominates the region of pulse overlap in ECMPI/MeOH because the cancellation of the ground and excited state terms persists for a greater  $T$  delay compared to ECMPI/MeCN. The experimental  $t_{\text{cm}}(T)$  evolve for  $T > 200$ , that is, after the pulses are no longer overlapped in the sample, whereas the calculated  $P_{\text{PORS}}^{(5)}(t, \tau, T)$  converges to and remains at a constant value by  $T = 200$  fs. The disagreement between the experiment and the theoretical model suggests that the relaxation of solvent structure in  $T$  alters the local distribution of vibrational modes and/or vibrational linewidths. Our model assumes linear response and does not allow for the mode distribution or their linewidths,  $\Gamma_j^m$ , to evolve in  $T$ .<sup>38</sup> Linear response is apparently a poor approximation for the solvated ECMPI systems. A nonequilibrium time-dependent spectral density representation is therefore required. Previous PORS<sup>25</sup> and RAPTORS<sup>28</sup> experiments also suggest that the assumption of linear response does not hold for Coumarin laser dyes solvated in acetonitrile.

#### D. Spectral evolution

The spectral density represents the distribution of reorganization energy (i.e., solute-solvent coupling strength) with respect to the frequency of nuclear motion. The PORS signal is linear in the reorganization energy under the assumption of small nuclear displacements.<sup>26</sup> The spectral evolution of  $E_s(\omega_t, \tau, T)$  reflects the redistribution of reorganization energy among various solvent motions as the system equilibrates. As discussed above,  $P_{\text{NR}}^{(5)}(t, \tau, T)$  gives rise to a strong dispersive response when the pulses are overlapped in the sample and therefore the spectral density is most directly obtained by considering the real signal component at short  $T$ . The representation considered in this section is useful for viewing general trends in the evolving spectral density for  $T$  at which the photoinitiating and Raman probe pulses are well separated (see Fig. 1).

Figure 5(a) presents the first moment of the experimental signal spectra obtained with

$$\bar{\Omega}_{rs}(\tau = 0, T) = \frac{\int_{-\infty}^{\infty} \omega_{rs} |E_s(\omega_t, \tau, T)| d\omega_t}{\int_{-\infty}^{\infty} |E_s(\omega_t, \tau, T)| d\omega_t}, \quad (33)$$

where  $\omega_{rs} = \bar{\omega}_{3,4} - \omega_t$ . The  $\bar{\Omega}_{rs}(T)$  for ECMPI in MeCN decrease from  $130 \text{ cm}^{-1}$  at  $T = 0$  fs to  $110 \text{ cm}^{-1}$  at  $T = 500$  fs. The  $\bar{\Omega}_{rs}(T)$  for ECMPI in MeOH is initially  $150 \text{ cm}^{-1}$  near  $T = 0$  then rapidly decreases for  $T > 200$  fs and finally converges to  $60 \text{ cm}^{-1}$  at  $T = 350$  fs. The calculated  $\bar{\Omega}_{rs}(T)$  associated with  $P_{\text{tot}}^{(5)}(t, \tau, T)$  in Fig. 9(a) exhibits a similar profile to the experimental data, particularly for ECMPI in MeOH. The rapid decrease in  $\bar{\Omega}_{rs}$  occurs in the range of  $T$  corresponding to the transition between  $P_{\text{NR}}^{(5)}(t, \tau, T)$  and  $P_{\text{PORS}}^{(5)}(t, \tau, T)$ . This interpretation is confirmed by the theoretical calculations presented in Fig. 9(b) in which the  $\bar{\Omega}_{rs}(T)$  associated with  $P_{\text{NR}}^{(5)}(t, \tau, T)$  and  $P_{\text{PORS}}^{(5)}(t, \tau, T)$  are displayed separately. The  $\bar{\Omega}_{rs}(T)$  for  $P_{\text{NR}}^{(5)}(t, \tau, T)$  decrease for  $T > 0$ , whereas the  $\bar{\Omega}_{rs}(T)$  associated with  $P_{\text{PORS}}^{(5)}(t, \tau, T)$  are inde-

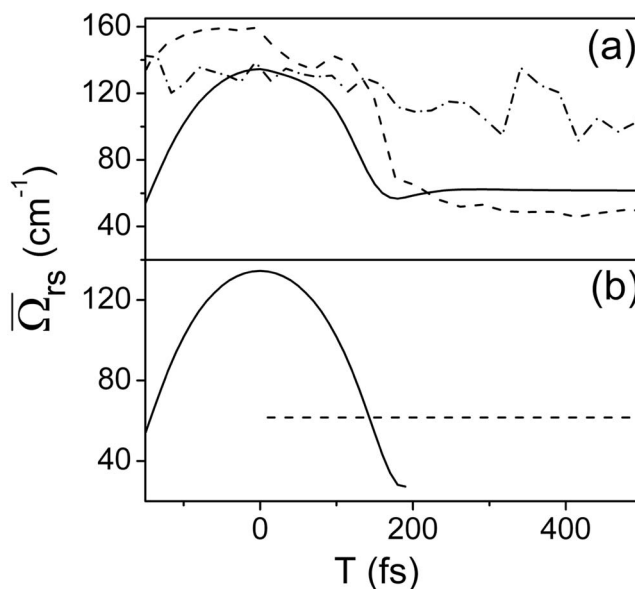


FIG. 9. (a) Experimental  $\bar{\Omega}_{rs}(T)$  [Eq. (33)] obtained for ECMPI in MeCN (dashed-dotted black) and MeOH (dashed black). Theoretical  $\bar{\Omega}_{rs}(T)$  computed with  $P_{\text{tot}}^{(5)}(t, \tau, T)$  (solid black). (b) Theoretical  $\bar{\Omega}_{rs}(T)$  [Eq. (33)] calculated for  $P_{\text{PORS}}^{(5)}(t, \tau, T)$  (dashed black) and  $P_{\text{NR}}^{(5)}(t, \tau, T)$  (solid black). The theoretical  $\bar{\Omega}_{rs}(T)$  are computed with the parameters given in Table I.

pendent of  $T$ . Note that  $\bar{\Omega}_{rs}(T)$  of  $P_{\text{tot}}^{(5)}(t, \tau, T)$  is not the average of the  $\bar{\Omega}_{rs}(T)$ 's for  $P_{\text{NR}}^{(5)}(t, \tau, T)$  and  $P_{\text{PORS}}^{(5)}(t, \tau, T)$  because the amplitudes of the latter two components are  $T$  dependent (see Fig. 7).

#### V. CONCLUSION

This paper presents our new full field-resolved implementation of PORS and explains the issues involved in its design and implementation. Signal detection by spectral interferometry is accomplished with the robust phase stability provided by a diffractive optic based interferometer. As discussed in Sec. III C, the signal of interest is obtained by combining a noncollinear beam geometry with a scheme for modulating the amplitudes of the individual beams. A major advantage to the present method over our previous apparatus<sup>25</sup> is that the measurement of the Raman response is performed in the frequency domain with fixed pulse delays giving 300 times faster data acquisition. In addition, the signal field is fully resolved to reveal signatures of nonresonant and Raman responses in the time-frequency shapes of the signals as well as the real and imaginary signal components. Our measurements show that the main limitation to viewing sub-100 fs dynamics in the present experiment is that the nonresonant response emits a strong background field when the pulses are overlapped in the sample. Recent applications of pulse shaping in coherent Raman spectroscopies suggest that the nonresonant contribution can be suppressed by modulating the phases of the Raman probe fields.<sup>68,69</sup>

This work is aimed at obtaining physical insight into the origin of the PORS response. Equations (24a)–(24c) and Fig. 3 describe the essential concepts. Our numerical calculations in Sec. IV capture the main features of the experimental signals but underestimate the rise time of  $P_{\text{PORS}}^{(5)}(t, \tau, T)$  be-

cause temporally well-separated photoinitiation and Raman probe events are assumed (see Fig. 1). As an alternative to the present approach, the region of the laser pulse overlap could be more accurately described with a theoretical model that explicitly integrates over  $t_1$ ,  $t_2$ , and  $t_4$  of Eq. (8); the  $t_3$  and  $t_5$  intervals can still be taken as instantaneous provided that the solution is transparent at the carrier frequencies of fields 3–6. Such a model could take full advantage of the dynamic range provided by spectral interferometry by relating material dynamics to the more subtle features of the signals. However, these additional insights would come at a significant increase in the computational expense because nested integrals would have to be evaluated.

The observed  $T$  dependence of the PORS line shape suggests that the approximation of linear response does not hold for the ECMPI systems. For this reason, we have assumed a phenomenological solvation correlation function,  $M_j(T)$ , to describe the overdamped relaxation of the nuclear coordinate in our model calculations. Overdamped motion in  $T$  is consistent with our data as recurrences in the signal amplitude and phase are not observed. Of course, this approximation may not hold for all systems. As demonstrated in a recent (fifth order) off-resonant femtosecond stimulated Raman study of deuterio-chloroform, it is essential to account for underdamped nuclear coherences in  $T$  because they cause recurrences in the signal phase, which reflect anharmonic couplings between nuclear modes.<sup>70</sup> Similarly, applications of PORS with shorter duration laser pulses, capable of exciting nuclear coherences in  $T$ , are expected to uncover signatures of anharmonic couplings between nuclear relaxation of the composite solute-solvent system in  $T$  and the solvent modes probed in  $t_4$ .

Our analysis suggests that a nonresonant response dominates the signal emission at short delays along the reaction time coordinate,  $T$ , for the ECMPI/MeOH system, whereas the resonant PORS response essentially rises with the convolution of the resonant pulse with the pulses of the Raman probe for ECMPI/MeCN. We interpret this difference as an indication that the electronic excitation-induced nuclear reorganization occurs on a much faster time scale for ECMPI/MeCN than ECMPI/MeOH, which is consistent with previous measurements of solvation time scales for these solvents.<sup>71</sup>

The present theoretical model has established that the experimentally observed evolution of the PORS line shapes in the reaction time,  $T$ , is a signature that the approximation of linear response does not hold for these systems. Further development of the PORS theoretical description will aim to go beyond the linear response approximations traditionally used to describe chemical reactions of solvated systems. The practical goal of these PORS measurements is to connect the time-evolving spectral densities to the reaction dynamics. We pursue this goal in another publication.<sup>26</sup>

## ACKNOWLEDGMENTS

We thank the National Science Foundation (CHE 0317009) for their support. N.F.S. acknowledges the John S.

Guggenheim Foundation for a Fellowship. R.A.N. thanks CAPES Brazil for a fellowship.

## APPENDIX A: COORDINATE DEPENDENCE OF THE POLARIZABILITY

The coordinate dependence of the PORS signal can be understood by expanding the polarizability as

$$\alpha[q_j^m(T)] = \alpha[q_j^m(T)] + \sum_j \alpha'[q_j^m(T)]q_j^m(T) + \dots, \quad (\text{A1})$$

where

$$\alpha'[q_j^m(T)] = \left( \frac{\partial \alpha}{\partial q_j} \right)_{q_j^m(T)}. \quad (\text{A2})$$

Equation (15) defines the coordinate  $q_j^m(T)$ . The derivative of the polarizability in Eq. (A2) is evaluated at the position of the coordinate,  $q_j$ , in state  $m$  at time  $T$ . To first order, the magnitude of the PORS correlation function for electronic state  $m$  [see Eq. (16)] is determined by the second term of Eq. (A1) because the commutator vanishes in the absence of coordinate dependence (i.e., the Condon approximation). By inserting the expansion of Eq. (A1) and keeping the leading term we obtain

$$\begin{aligned} \Phi_j^m(t_4, T) &= \frac{i|\mu_{eg}|^2}{\hbar^5} [1 - \exp(-\beta\hbar\omega_j)] \exp[(i\omega_j - \Gamma_j^m)t_4] \\ &\times \int_{-\infty}^{\infty} dq_j |\alpha'[q_j^m(T)]|^2 D_j^m(q_j, T). \end{aligned} \quad (\text{A3})$$

Our numerical calculations in Sec. IV take  $\alpha'[q_j^m(T)]$  to be linear in the coordinate as given in Table I.

## APPENDIX B: SPECTRUM OF FIELD 5

The experimental spectrum of field 5 does not have a Gaussian shape. The numerical calculations are performed by assuming the following functional form:

$$\hat{\xi}_6(\mathbf{k}_6, \omega) = \exp[-a(\omega' - \omega)^2], \quad (\text{B1})$$

where  $a = \delta t^2 / 16 \ln(2)$  and  $\delta t$  is the FWHM of  $\hat{\xi}_6(\mathbf{k}_6, \omega)$ . The shape is obtained by assuming that  $\delta t = 120$  fs for  $\omega < \omega'$  and  $\delta t = 225$  fs for  $\omega > \omega'$ . The frequency,  $\omega'$ , is redshifted by  $96 \text{ cm}^{-1}$  with respect to the carrier frequency of the 3, 4 field pair,  $\bar{\omega}_{3,4}$ , for the calculations presented in Sec. IV.

<sup>1</sup>H. A. Kramers, *Physica (Utrecht)* **7**, 284 (1940).

<sup>2</sup>J. E. Straub, M. Berkovec, and B. J. Berne, *J. Chem. Phys.* **83**, 3172 (1985).

<sup>3</sup>J. E. Straub, M. Berkovec, and B. J. Berne, *J. Chem. Phys.* **84**, 1788 (1986).

<sup>4</sup>R. F. Grote and J. T. Hynes, *J. Chem. Phys.* **73**, 2715 (1980).

<sup>5</sup>R. F. Grote and J. T. Hynes, *J. Chem. Phys.* **74**, 4465 (1981).

<sup>6</sup>E. Pollak, *J. Chem. Phys.* **85**, 865 (1986).

<sup>7</sup>A. Nitzan, *Adv. Chem. Phys.* **70**, 489 (1988).

<sup>8</sup>C. Reichardt, *Solvents and Solvent Effects in Organic Chemistry* (VCH, New York, 1990).

<sup>9</sup>P. Hänggi, P. Talkner, and M. Borkovec, *Rev. Mod. Phys.* **62**, 251 (1990).

<sup>10</sup>G. R. Fleming and P. Hänggi, *Activated Barrier Crossing* (World Scientific, Singapore, London, Hong Kong, 1993).

<sup>11</sup>C. H. Brito-Cruz, R. L. Fork, W. H. Knox, and C. V. Shank, *Chem. Phys. Lett.* **132**, 341 (1986).

<sup>12</sup>T. J. Kang, Y. Jongwan, and M. Berg, *J. Chem. Phys.* **94**, 2413 (1991).

- <sup>13</sup>H. Murakami, S. Kinoshita, Y. Hirata, T. Okada, and N. Mataga, *J. Chem. Phys.* **97**, 7881 (1992).
- <sup>14</sup>W. P. de Boeij, M. S. Pshenichnikov, and D. A. Wiersma, *Annu. Rev. Phys. Chem.* **49**, 99 (1998).
- <sup>15</sup>M. J. Lang, X. J. Jordanides, X. Song, and G. R. Fleming, *J. Chem. Phys.* **110**, 5884 (1999).
- <sup>16</sup>P. Voehringer and N. F. Scherer, *J. Phys. Chem.* **99**, 2684 (1995).
- <sup>17</sup>L. D. Book and N. F. Scherer, *J. Chem. Phys.* **111**, 792 (1999).
- <sup>18</sup>W. Qian and D. M. Jonas, *J. Chem. Phys.* **119**, 1611 (2003).
- <sup>19</sup>W. Jarzeba, G. C. Walker, A. E. Johnson, M. E. Kahlow, and P. F. Barbara, *J. Phys. Chem.* **92**, 7039 (1988).
- <sup>20</sup>M. A. Kahlow, W. Jarzeba, T. J. Kang, and P. F. Barbara, *J. Chem. Phys.* **90**, 151 (1989).
- <sup>21</sup>S. J. Rosenthal, X. Xie, M. Du, and G. R. Fleming, *J. Chem. Phys.* **95**, 4715 (1991).
- <sup>22</sup>R. Jimenez, G. R. Fleming, P. V. Kumar, and M. Maroncelli, *Nature (London)* **369**, 471 (1994).
- <sup>23</sup>L. Reynolds, J. A. Gardecki, J. V. Frankland, M. L. Horng, and M. Maroncelli, *J. Phys. Chem.* **100**, 10337 (1996).
- <sup>24</sup>S. Park, J. Kim, and N. F. Scherer, *Ultrafast Phenomena XIV* (Springer-Verlag, Berlin, 2005), Vol. 79.
- <sup>25</sup>S. Park, A. M. Moran, J. Kim, and N. F. Scherer (in preparation, 2007).
- <sup>26</sup>A. M. Moran, R. A. Nome, S. Park, and N. F. Scherer (submitted to *Phys. Rev. Lett.*, 2007).
- <sup>27</sup>D. F. Underwood and D. A. Blank, *J. Phys. Chem. A* **107**, 956 (2003).
- <sup>28</sup>D. F. Underwood and D. A. Blank, *J. Phys. Chem. A* **109**, 3295 (2005).
- <sup>29</sup>S. J. Schmidtke, D. F. Underwood, and D. A. Blank, *J. Phys. Chem. A* **109**, 7033 (2005).
- <sup>30</sup>D. W. McCamant, P. Kukura, and R. A. Mathies, *J. Phys. Chem. A* **107**, 8208 (2003).
- <sup>31</sup>P. Kukura, D. W. McCamant, and R. A. Mathies, *J. Phys. Chem. A* **108**, 5921 (2004).
- <sup>32</sup>D. W. McCamant, P. Kukura, S. Yoon, and R. A. Mathies, *Rev. Sci. Instrum.* **75**, 4971 (2004).
- <sup>33</sup>P. Kukura, D. W. McCamant, S. Yoon, D. B. Wandschneider, and R. A. Mathies, *Science* **310**, 1006 (2005).
- <sup>34</sup>S. Laimgruber, H. Schachenmayr, B. Schmidt, W. Zinth, and P. Gilch, *Appl. Phys. B: Lasers Opt.* **85**, 557 (2006).
- <sup>35</sup>S. Park, Ph.D. thesis, The University of Chicago, 2006.
- <sup>36</sup>A. M. Moran, S. Park, and N. F. Scherer, *J. Phys. Chem. B* **110**, 19771 (2006).
- <sup>37</sup>A. M. Moran, R. A. Nome, and N. F. Scherer, *J. Chem. Phys.* **125**, 031101 (2006).
- <sup>38</sup>A. M. Moran, S. Park, and N. F. Scherer, *Chem. Phys.* **341**, 344 (2007).
- <sup>39</sup>A. R. Bogdan, M. W. Downer, and N. Bloembergen, *Phys. Rev. A* **24**, 623 (1981).
- <sup>40</sup>J. R. Andrews and R. M. Hochstrasser, *Chem. Phys. Lett.* **82**, 381 (1981).
- <sup>41</sup>L. J. Rothberg and N. Bloembergen, *Phys. Rev. A* **30**, 820 (1984).
- <sup>42</sup>S. Mukamel, *Principles of Nonlinear Optical Spectroscopy* (Oxford University Press, New York, Oxford, 1995).
- <sup>43</sup>G. D. Scholes, *J. Chem. Phys.* **121**, 10104 (2004).
- <sup>44</sup>V. M. Huxter, V. Kovalevskij, and G. D. Scholes, *J. Phys. Chem. B* **109**, 20060 (2005).
- <sup>45</sup>G. D. Scholes, J. Kim, and C. Y. Wong, *Phys. Rev. B* **73**, 195325 (2006).
- <sup>46</sup>A. M. Moran, R. A. Nome, and N. F. Scherer, *J. Phys. Chem. A* **110**, 10925 (2006).
- <sup>47</sup>Y. J. Yan, L. E. Fried, and S. Mukamel, *J. Phys. Chem.* **93**, 8149 (1989).
- <sup>48</sup>M. A. Herschberger, A. M. Moran, and N. F. Scherer (research in progress, 2007).
- <sup>49</sup>K. A. Nelson, R. Casalegno, R. J. D. Miller, and M. D. Fayer, *J. Chem. Phys.* **77**, 1144 (1982).
- <sup>50</sup>J. D. Hybl, A. Yu, D. A. Farrow, and D. M. Jonas, *J. Phys. Chem. A* **106**, 7651 (2002).
- <sup>51</sup>L. Lepetit, G. Chéiaux, and M. Joffre, *J. Opt. Soc. Am. B* **12**, 2467 (1995).
- <sup>52</sup>C. Dorrer, N. Belabas, J. P. Likforman, and M. Joffre, *J. Opt. Soc. Am. B* **17**, 1795 (2000).
- <sup>53</sup>E. Tokunaga, A. Terasaki, and T. Kobayashi, *J. Opt. Soc. Am. B* **12**, 753 (1995).
- <sup>54</sup>S. M. Gallagher, A. W. Albrecht, J. D. Hybl, B. L. Landin, B. Rajaram, and D. M. Jonas, *J. Opt. Soc. Am. B* **15**, 2338 (1998).
- <sup>55</sup>R. Trebino, *Frequency Resolved Optical Gating: The Measurement of Ultrashort Laser Pulses* (Kluwer Academic Publishers, Boston, Dordrecht, London, 2000).
- <sup>56</sup>M. Khalil, N. Demirdöven, and A. Tokmakoff, *J. Phys. Chem. A* **107**, 5258 (2003).
- <sup>57</sup>N. Belabas and D. M. Jonas, *J. Opt. Soc. Am. B* **22**, 655 (2005).
- <sup>58</sup>T. Brixner, I. V. Stiopkin, and G. R. Fleming, *Opt. Lett.* **29**, 884 (2004).
- <sup>59</sup>A. M. Moran, J. B. Maddox, J. W. Hong, J. Kim, R. A. Nome, G. C. Bazan, S. Mukamel, and N. F. Scherer, *J. Chem. Phys.* **124**, 194904 (2006).
- <sup>60</sup>G. D. Goodno, G. Dadusc, and R. J. D. Miller, *J. Opt. Soc. Am. B* **15**, 1791 (1998).
- <sup>61</sup>G. D. Goodno and R. J. D. Miller, *J. Phys. Chem. A* **103**, 10619 (1999).
- <sup>62</sup>G. D. Goodno, V. Astinov, and R. J. D. Miller, *J. Phys. Chem. A* **103**, 10630 (1999).
- <sup>63</sup>N. F. Scherer, R. J. Carlson, M. Du, A. J. Ruggiero, A. Matro, V. R. Rochin, J. A. Cina, and G. R. Fleming, *J. Chem. Phys.* **95**, 1487 (1991).
- <sup>64</sup>J. P. Likforman, M. Joffre, and V. Thierry-Mieg, *Opt. Lett.* **22**, 1104 (1997).
- <sup>65</sup>T. Brixner, T. Mancal, I. V. Stiopkin, and G. R. Fleming, *J. Chem. Phys.* **121**, 4221 (2004).
- <sup>66</sup>A. M. Moran, J. B. Maddox, J. W. Hong, J. Kim, R. A. Nome, G. C. Bazan, S. Mukamel, and N. F. Scherer, *Ultrafast Phenomena XV* (Springer-Verlag, Berlin, 2007).
- <sup>67</sup>S. D. McGrane, R. J. Scharff, and J. Barber, *J. Opt. Soc. Am. B* **23**, 2217 (2006).
- <sup>68</sup>N. Dudovich, D. Oron, and Y. Silberberg, *J. Chem. Phys.* **118**, 9208 (2003).
- <sup>69</sup>S. H. Lim, A. G. Caster, O. Nicolet, and S. R. Leone, *J. Phys. Chem. B* **110**, 5196 (2006).
- <sup>70</sup>P. Kukura, R. Frontiera, and R. A. Mathies, *Phys. Rev. Lett.* **96**, 238303 (2006).
- <sup>71</sup>M. L. Horng, J. A. Gardecki, and M. Maroncelli, *J. Phys. Chem.* **99**, 17311 (1995).